Journal of
Ship&Ocean
Technology
©SEPTEMBER 2008

SOTECH Vol. 12, No. 3, pp. 14 ~ 25, 2008

Experimental and Improved Numerical Studies on Aerodynamic Characteristics of Low Aspect Ratio Wings for a Wing-In Ground Effect Ship

Byoung-Kwon Ahn[1], Hyung-Tae Kim[1], Chang-Sup Lee[1] and Jae-Moon Lew[1]

[1] Department of Naval Architecture and Ocean Engineering, Chungnam National University, Chungnam, Korea;
Corresponding Author: bkahn@cnu.ac.kr

Abstract

Recently, there has been a serious effort to design a wing in ground effect (WIG) craft. Vehicles of this type might use low aspect ratio wings defined as those with smaller than 3. Design and prediction techniques for fixed wings of relatively large aspect ratio are reasonably well developed. However, Aerodynamic problems related to vortex lift on wings of low aspect ratio have made it difficult to use existing techniques. In this work, we firstly focus on understanding aerodynamic characteristics of low aspect ratio wings and comparing the results from experimental measurements and currently available numerical predictions for both inviscid and viscous flows. Second, we apply an improved numerical method, "B-spline based high order panel method with wake roll-up modeling", to the same problem.

Keywords: low aspect ratio wing, aerodynamics, vortex lift, induced drag, B-spline high order panel method

1 Introduction

As demands for high speed sea transportations have recently been increased, various high speed ships appear. Among them the WIG (Wing-In Ground Effect) craft is believed to be the next generation of the sea transportation system. Development of the large WIG craft is now competitively ongoing around the world including Korea, and it is expected to be commercialized in the near future. It is, therefore, supposed that the needs for related various researches on the WIG craft will be continuously required.

Low aspect ratio wing generally is used as a main wing of the WIG craft because of its effective aerodynamic characteristics. When the flow separates at the leading edge of low aspect wings, a vortex was developed along the tip side leading edge which produces an increase in lift referred to as "vortex lift". A widely accepted explanation of this vortex flow phenomenon is the leading edge suction (Polhamus 1957). Experiments show that leading edge separation rolls up into a vortex near the wing tip, and progressively extends as the angle of attack increases. Its typically well-known example is the leading edge vortex of delta wings in which vortices exert a large influence on the lift characteristics

(Polhamus 1957). The suction analogy can provides prediction of the vortex flow characteristics of slender sharp edge delta wings. The pressure differential between the upper and lower sides causes the flow velocity and the formation of the leading edge vortices. As would be expected the pressure difference increases with angle of attack with a resultant increase in the strength of the vortices. Lamar (1974) extended the analogy to a variety of bodies with round leading edges. Greeley and Kerwin (1982) applied an empirical correction of the leading edge suction force to propeller lifting problem.

Over the past few decades a large number of different potential based methods have been developed and successfully used as a useful tool for aerodynamic and hydrodynamic designs. Lifting-surface theory represents very well for the wings with aspect ratios above AR=5. The influence of the lateral edge becomes more and more dominant as the aspect ratio approaches zero. Empirical corrections are well applied in some practical cases, but there are still discrepancies between numerical predictions of small aspect ratio wings. The existing panel methods treat the velocity potential as constant or discontinued high order over a panel. This assumption inevitably results in numerical differentiation errors, which are significant near the tip and at the trailing edge region of the wing. Recently a high order panel method based on a B-spline has been developed and widely applied. The order of the B-splines to represent both the body geometry and the velocity potential can be increased without limit and discontinuity, and hence the solution of any order can be obtained. Detailed information on the B-spline based method for two dimensional cases is available from Kerwin and Newman (1993). Lee and Kerwin (2003) introduced numerical procedures for the analysis of two-dimensional foils. Kim et al (2007) extended them to three-dimensional bodies.

In the work, we carried out experimental measurements of aerodynamics characteristics of several low aspect ratio wings in a wind tunnel and compared them with an improved numerical analysis using a B-spline based high order panel method. Trailing wake alignment procedures satisfying the kinematic and dynamic boundary conditions on a shedding wake surface have been investigated by taking a close look at the case of the low aspect ratio wing and new wake roll-up procedure were adopted.

2 Experimental measurements

The tests were performed in a 0.4x0.4 meter open type wind tunnel in the Division of Aerospace, Naval Architecture and Ocean Engineering at Chungnam National University. The tunnel inlet contains a honeycomb flow straightener and the units are situated on rubber mounts to minimize vibration. Flow speeds of between 10 and 20 m/s were used in the work. Fixed tunnel speeds were selected to give the desired Reynolds number from 105 to 106.

Figure 1 shows experimental apparatus setup. Force measures were made using a six-component strain gauge balance constructed specially for the work. The balance was calibrated using precision weights connected to the balance mounting point by wires. The wires were aligned to the horizontal and vertical using spirit levels and by sighting the wires against known vertical and horizontal features of the tunnel. Lift and drag measurements were available in real time on the displays. Uniformity of the outflow was measured and Figure 2 shows a plot of the velocity profile measured at 10m/s and 20m/s.

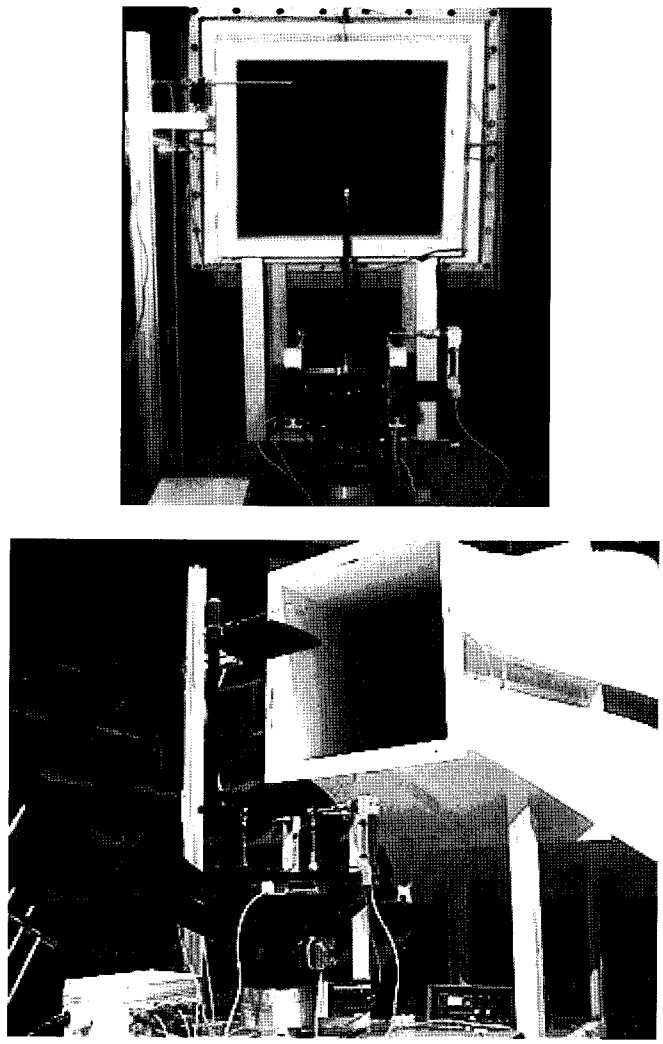

Figure 1: Experimental setup

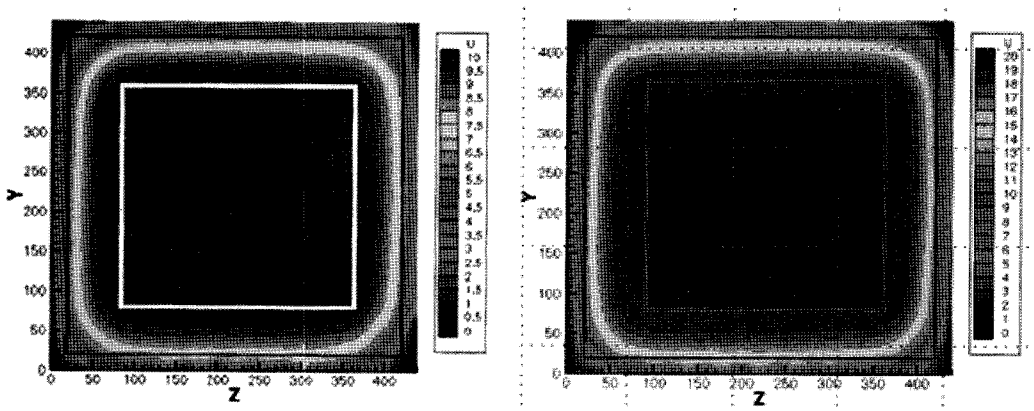

Figure 2: Cross sectional uniformity of the outflow (top: 10m/s, bottom: 20 m/s)

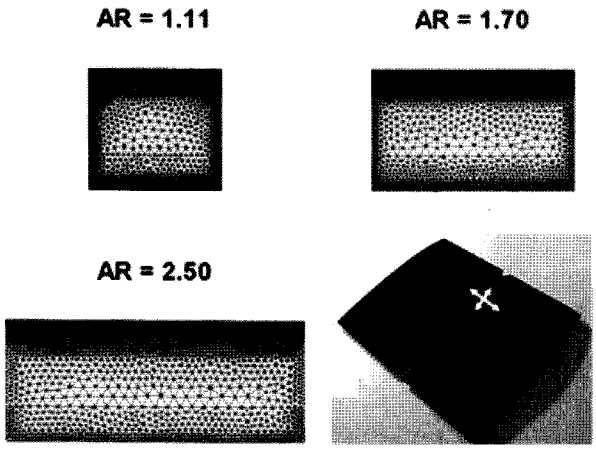

Figure 3: Test wings

A base model NACA0012 aerofoil of chord 135mm and span 150mm (AR=1.11) was used, and two different wings (AR=1.70 and 2.50) were constructed. The model was mounted vertically and attached to the force balance sting through a sting arm in the trailing edge of the model (see Figure 1). 2500 experimental data were acquired per channel at a frequency of 5 kHz for 10 seconds. The angle of attack of the model was varied from -10 to 20 degree using a computer controlled stepper motor. Flow visualization was planned to gain a qualitative understanding of tip flow behavior of the low aspect wing. Unfortunately, no photographs are available to date because of lighting problems.

3 Numerical formulations

3.1 B-spline representation and Integral equation

The potential is represented as a weighted sum of tensor product B-spline basis functions in a similar form as for the geometry as $\phi(u,v)$ along the surface of the body. However, instead of treating the potential directly, we represent the potential as a weighted sum of tensor product B-spline basis functions in a similar form as for the geometry:

$$\phi(u,v) = \sum_{i=0}^{N^v-1} \sum_{j=0}^{M^v-1} \phi_{i,j}^v N_i(u) M_j(v) \tag{1}$$

where $N_i(u)$ and $M_j(v)$ are the B-spline basis functions, $\phi_{i,j}^v$ the potential control vertices, and N^v and M^v the numbers of potential control vertices in u,v directions respectively. The numbers of potential control vertices (N^v, M^v) and the basis functions $(N_i(u), M_j(v))$ may be different from the corresponding quantities for the geometry, but usable parametric spaces of the geometry and potentials should be identical. With the introduction of the potential vertices, the unknowns of the hydrodynamic problem are now

values of the potential vertices $\phi^{v}_{i,j}$ that are not the potential in the physical sense. The potential knot vectors in (u,v) are defined:

$$\begin{aligned}\vec{U} &= \{0,0,0,0,1/N^{\phi},2/N^{\phi},\cdots,1,1,1,1,\}^{T}\\ \vec{V} &= \{0,0,0,0,1/M^{\phi},2/M^{\phi},\cdots,1,1,1,1\}^{T}\end{aligned} \tag{2}$$

The numbers of spans or panels in (u,v)-directions in usable parametric spaces for the potential are (N^{ϕ},M^{ϕ}) and they are related with the number of potential control vertices in forms of $N^{v}=N^{\phi}+p$ and $M^{v}=M^{\phi}+q$.

The potential on the body surface is represented by the influences of the normal dipoles and the sources distributed on the body surface consisting of the body and the wake surface as

$$\frac{\phi}{2}=\iint_{S_B}\left[\frac{\partial\phi}{\partial\bar{n}}G-\phi\frac{\partial G}{\partial\bar{n}}\right]ds-\iint_{S_W}\Delta\phi\frac{\partial G}{\partial\bar{n}}dS \tag{3}$$

where ϕ is the perturbed velocity potential, $\bar{n}$ the unit normal vector of the body and wake surface, and G the Green function. Discretization into a set of (N^{ϕ},M^{ϕ}) panels on the body and M^{ϕ} strips in wake yields

$$\begin{aligned}&\frac{\phi}{2}+\sum_{\upsilon,\mu}\iint_{S_{\upsilon,\mu}}\phi\frac{\partial G}{\partial n}ds+\sum_{\mu}\iint_{S^{w}_{\mu}}(\Delta\phi)_{\mu}\frac{\partial G}{\partial n}ds\\ &=\sum_{\upsilon,\mu}\iint_{S_{\upsilon,\mu}}\frac{\partial\phi}{\partial n}GdS\end{aligned} \tag{4}$$

Depending on the relative position of the control point to the singular panel, induction integrals are devided into self-induction, near-field induction and far-field induction integrals. Noting that there are only $(p+1,\ q+1)$ nonzero basis functions at each span defined by the space between adjacent knots in (2), we may rewrite the potential (1) as a $(p+1,q+1)$ term summation:

$$\phi(u,v)=\sum_{a=0}^{p}\sum_{b-0}^{q}\phi^{v}_{\alpha,\beta}N_{\alpha}(u)M_{\beta}(v) \tag{5}$$

where subscripts (s,t) are span indices satisfying the relation $(u,v)\in((u_s,u_{s+1}),(v_t,v_{t+1}))$ in the knot vectors (2), $\alpha=s-p+a$ and $\beta=t-q+b$. Substitution of the equation (5) into (4) gives the control point on (i, j)-th panel:

where $\alpha_i=s_i-p+a$, $\beta_i=t_i-q+b$, $\alpha=s_v-p+a$ and $\beta=t_{\mu}-q+b$. It should be noticed that the (υ,μ) summation for the dipole over the panels in (6) includes cases $i=\upsilon$ and $j=\mu$. In the low order panel method, these terms are eliminated, since the effect is already considered by the subtended angle of the hemisphere surrounding the point where the potential is evaluated. In the higher-order panel method, there are additional effects from

the curvature of the geometry and the higher order variation of the potential in addition to the subtended angle effect.

$$\begin{aligned}&\frac{1}{2}\{\sum_{a,b} N_{a_i}(u_i)M_{\beta_i}(v_i)\phi^v_{\alpha_i,\beta_i}\}\\&+\sum_{\upsilon,\mu}\iint_{S_{\upsilon,\mu}}\{\sum_{a,b} N_\alpha(u)M_\beta(v)\phi^v_{\alpha,\beta}\}\frac{\partial G}{\partial n}dS\\&+\sum_{\mu}\iint_{S^w_\mu}(\Delta\phi)_\mu\frac{\partial G}{\partial n}dS=\sum_{\upsilon,\mu}\iint_{S_{\upsilon,\mu}}\frac{\partial\phi}{\partial n}GdS\end{aligned} \tag{6}$$

Depending on the relative position of the control point to the singularity panel, induction integrals are divided into self-induction, near-field induction and far-field induction integrals. Self-inductions due to high order normal dipole and source distributions are evaluated by Gaussian quadrature through avoiding the singularity. By adjusting the degree of the quadrature, induction integrals are able to reach any desired accuracy. When the control point falls very close to the panel, a continuous subdivision method can be applied to evaluate induction-integrals. Sub-divisions into smaller panels do not lose the accuracy of the geometry and the potential representations. Kutta condition is the zero pressure jump condition on the wake sheet. It is equivalent to the statement that magnitudes of the total velocity on both sides of the trailing edge should be identical in the steady flow.

$$(\vec{U}_r+\nabla\phi^+)^2=(\vec{U}_r+\nabla\phi^-)^2 \tag{7}$$

The simultaneous equation for determination of the potential is over-determined and it is solved using the least square method with the dynamic Kutta condition as constraints.

3.2 Wake alignment and roll-up

Applying the Green's theorem, the induced velocity can be obtained:

$$\begin{aligned}\nabla_p\phi(p)=&\iint_{S_B}\frac{\partial\phi}{\partial n_q}\nabla_p G-\phi(q)\nabla_p\left(\frac{\partial G}{\partial n_q}\right)dS\\&-\iint_{S_W}\Delta\phi(q)\nabla_p\left(\frac{\partial G}{\partial n_q}\right)dS\end{aligned} \tag{8}$$

Equation (7) represents that the induced velocity due to the body and the wake can be calculated by distributing dipoles and sources on the body and dipoles on the wake.

Figure 4 shows the procedure of the wake alignment. The wake can be aligned as the force-free condition is satisfied on each wake panel. After finding new positions vectors of wake panels, each panel moves into new position and rolls up (see Figure 5).

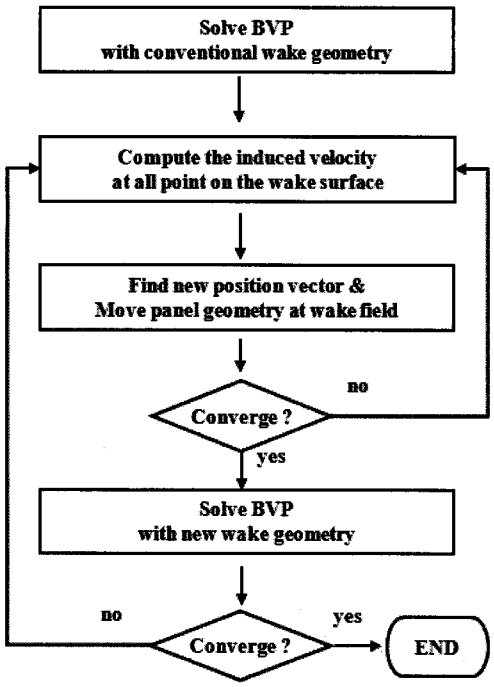

Figure 4: Procedure of the wake alignment

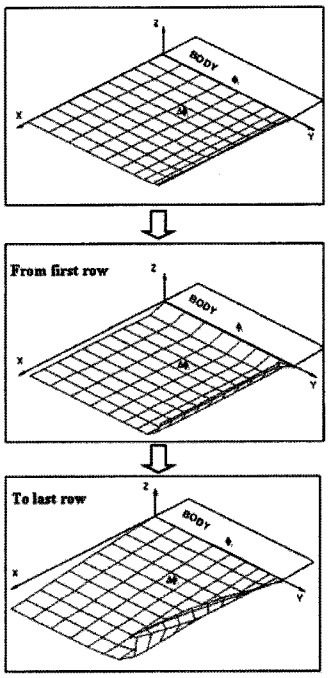

Figure 5: Schematic views of wake roll-up

4 Results and discussion

4.1 Preliminary numerical results

First, we considered a circular wing having 10% thickness at the mid-span and zero thickness at the tip. Applying wake alignment, trailing wake is investigated. Figure 6 shows cross sectional views of the wake roll-up at different downstream locations indicated in each position.

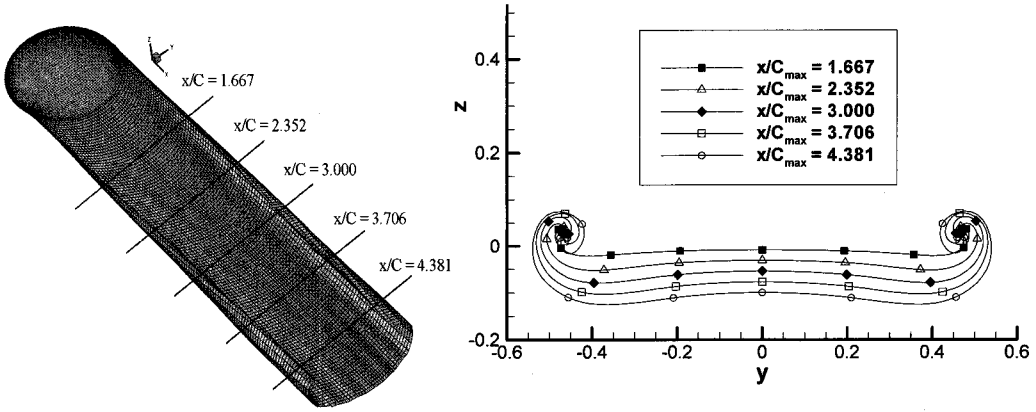

Figure 6: Circular wing and wake roll-up (t/c=0.1, α=5°)

4.2 Key comparison issues

Figure 7 and 8 show measured lift and drag forces for a rectangular wing (NACA0012 section, AR=1.11) at wind speed 6 to 18 m/s. The lift and drag were determined for both increasing and decreasing angles of attack to check for asymmetric behavior or hysteresis.

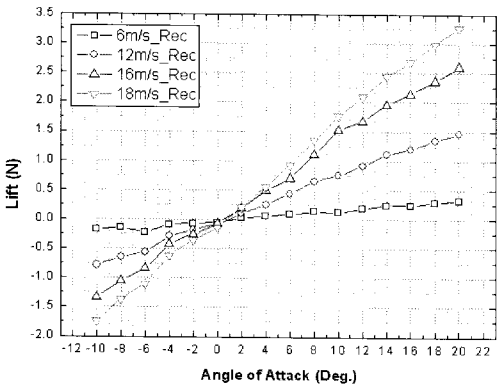

Figure 7: Lift measurements (AR=1.11)

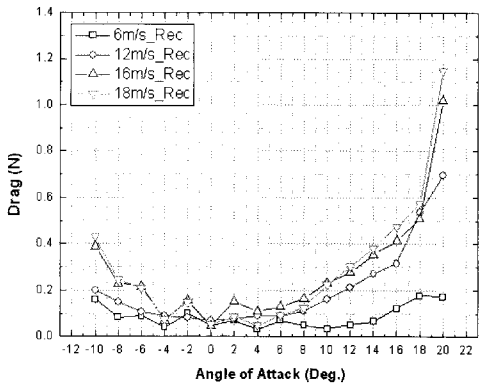

Figure 8: Drag measurements (AR=1.11)

Figure 9 shows comparison of lift and drag coefficients between experiments and numerical results. In cases of large aspect ratio wings, it is well known that predicted lift of inviscid flow is larger than the experiments because of elimination of viscous effect. However, as can be seen from Figure 9, experimental results are larger than invisicd solutions. As mentioned previous chapter, leading edge vortex developed at the tip side of low aspect wings produces an increase in lift. In order to complement the discrepancy between experimental and numerical results, in the work we modeled trailing wake roll-up mechanism using B-spline baed high order panel method and it gave improved results.

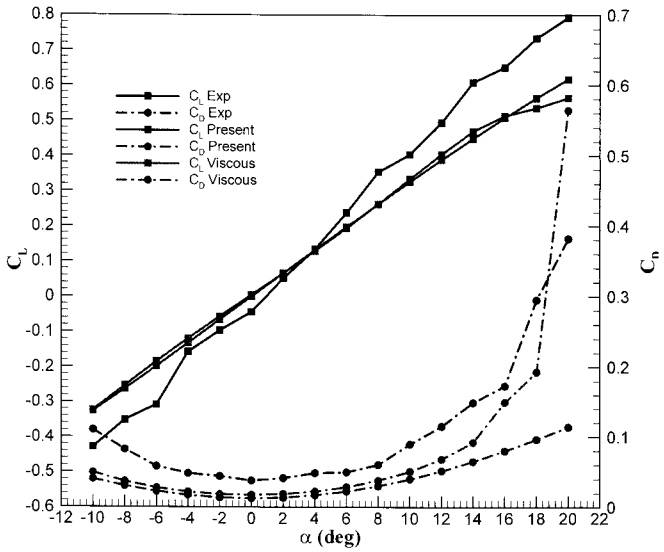

Figure 9: Comparison of lift and drag coefficients of the rectangular wing (AR=1.11)

4.3 Effects of the aspect ratio

Figure 10 shows lift and drag coefficients versus angle of attack according to different aspect ratios (AR=1.11, 1.70 and 2.5). Here the friction coefficient of the flat plate (C_f

=0.0045) was used for consideration of the viscous effect. One way of comparing the different effects of the aspect ratio is to compare their lift curve slopes. The slope of the C_L versus angle of attack of each model was calculated by applying the present method. Only the values of the lift coefficient corresponding to the attack angle between -10 to 10 degree were considered to assure that the lift curve behaved linearly (see Figure 10). In addition, obtained lift coefficients were compared to a number of theoretical predictions of the lift curve slope. The first one by Anderson (1991) is:

$$C_{L\alpha} = \frac{a_0}{1+\left(a_0 \times 57.3 / \pi AR\right)(1+\tau)} \tag{9}$$

where τ varies typically between 0.05 and 0.25, and a_0=0.094 was used.

Lowry and Polhamus (1957) proposed the theoretical equation supposed to be more accurate for small aspect ratios which is less than AR=2:

$$C_{L\alpha} = \left(\frac{1}{57.3}\right)\frac{2\pi AR}{2+\sqrt{AR^2/\eta^2\left(1+\tan^2\beta\right)+4}} \qquad \eta = \frac{C_{L\alpha(\text{foil})}}{2\pi} \tag{10}$$

where β is the sweep angle. Hoerner and Borst (1975) suggested the different lift curve slope of low aspect ratios, less than 2.5:

$$C_{L\alpha} = \left(\frac{36.5}{AR} + 2AR\right)^{-1} \tag{11}$$

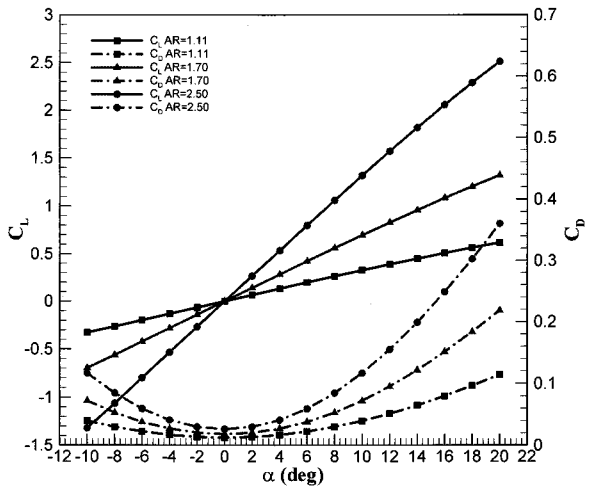

Figure 10: Lift and drag coefficients according to different aspect ratios

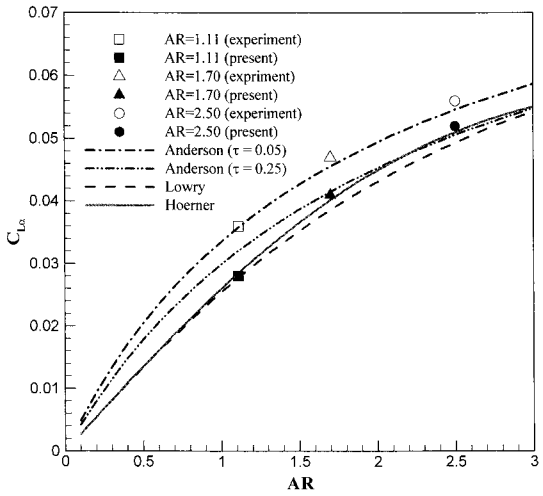

Figure 11: Lift curve slope ($C_{L\alpha}$) versus AR

In Figure 11, lift curve slopes for the models are compared with approximations of equations (9), (10) and (11). It can be concluded that equation (11) by Hoerner and Borst provides a good approximation of the lift curve slope for the present results.

Figure 12 shows pressure coefficients resulted from the low order panel (LoPan) and the present (HiPan) are compared for AR=1.11 and 2.5 cases with α=4°. The most significant differences arise near the tip region where pressure varies drastically in both cases due to the abrupt change of both geometry and flow characteristics. In the present method the solution in this region may provide critical information on the effect of tip vortex flow which exerts a large influence on the lift characteristics of low aspect ratio wings. Figure 13 show pressure distributions on suction sides of each wing.

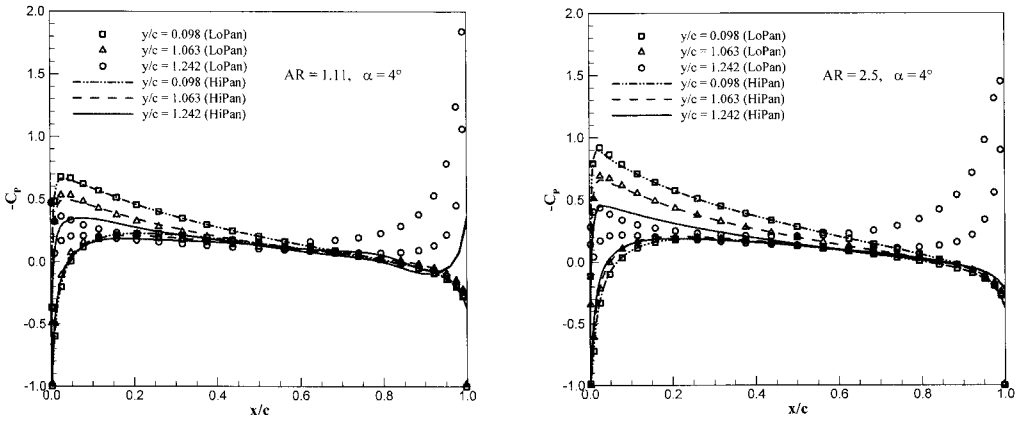

(a) AR=1.11, α=4° (b) AR=2.5, α=4°

Figure 12: Comparison of pressure coefficients at different span-wise locations (AR=2.5, α=4°)

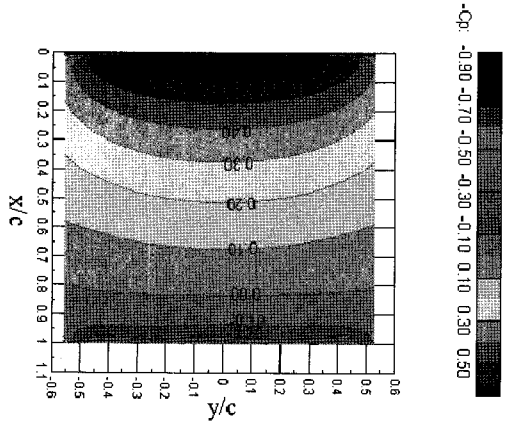

(a) AR=1.11, α=4°

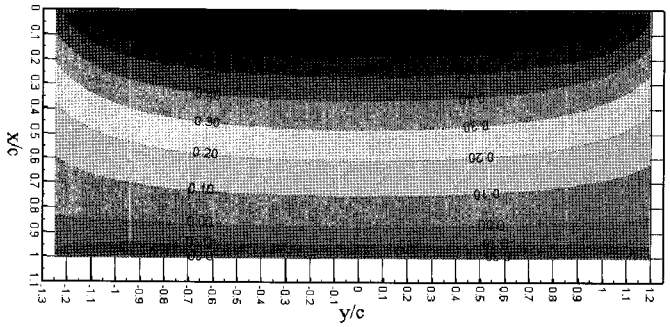

(b) AR=2.5, α=4°

Figure 13: Pressure distributions on the suction side of the wing

5 Conclusions and future work

In the present work, we focused our attention on aerodynamic characteristics of small aspect ratio wings. We first carried out experimental measurements of several low aspect ratio wings in a wind tunnel. On the purpose to complete the discrepancy between the results of experimental and low order panel method, we applied a B-spline based high order panel method and considered trailing wake roll-up mechanism. The presented results show more improved solutions comparing with existing prediction methods. Experimental measurements for different small aspect ratio wings and further numerical studies on them are now ongoing. To get more insight into the very complex flow of low aspect ratio wings, the leading edge separation phenomena will be further studied by applying different flow visualization techniques.

Acknowledgements

This work was carried out with the support of the Korea Science and Engineering Foundation (KOSEF) under Grant No. R01-2008-000-20852-0.

References

Anderson, J.D.J. 1991. Fundamentals of Aerodynamics, McGraw Hill, New York.

Greeley, D.S. and J.E. Kerwin. 1982. Numerical methods for propeller design and analysis in steady flow, Trans. SNAME, **90**.

Hoerner, S.F. and H. V. Borst. 1975. Fluid Dynamic Lift, Hoerner Fluid Dynamics, Brick Town, NJ, pp. 171-175.

Kim, G.D., B.K. Ahn, B.G. Paik, W.S. Lee and C.S. Lee. 2007. Numerical modeling of propeller tip flow with wake sheet roll-up by B-spline higher-order panel method. 10th International Symposium on Pratical Design of Ship and Other-Floating Structures, **2**, 517-522.

Lamar, J.E. 1974. Extension of the leading-edge suction analogy to wings with separated flow around the side edge at subsonic speeds, Technical Report TR-R-428, NASA.

Lee, C.-S. and J.E. Kerwin. 2003. A B-Spline higher order panel method applied to two-dimensional lifting problem, Journal of Ship Research, **47**, **4**, 290-298.

Lowry, J.G. and E.C. Polhamus. 1957. A Method for Predicting Lift Increments due to Flap Deflection at Low Angles of Attack in Incompressible Flow. Technical Report NACA TN-3911.

Polhamus. 1957. Vortex Lift Based on Leading -edge Suction Analogy, NASA TN D-3767.

Polhamus. 1957. Application of Leading-edge Suction Analogy for Delta Wings, NASA TN D-4739.